Smart Piezoelectric Sensors to monitor Concrete Strength for Enhanced Infrastructure Maintenance

Trushna Jena[1], T. Jothi Saravanan[1]* and Tushar Bansal[2]

[1]School of Infrastructure, Indian Institute of Technology Bhubaneswar, Odisha, India
[2]Department of Civil Engineering, Sharda University, Uttar Pradesh, India
**E-mail: tjs@iitbbs.ac.in*

ABSTRACT

The electromechanical impedance (EMI) technique has emerged as a powerful tool for structural health monitoring (SHM), yet the effectiveness of different piezoelectric sensor configurations in reinforced concrete remains inadequately understood. This study presents a combined experimental–numerical investigation of three sensor setups: surface-bonded (SBPS), embedded (EPS), and non-bonded (NBPS). Conductance–frequency analysis revealed that EPS exhibited the highest sensitivity, with resonance peaks shifting to 220–240 kHz as concrete stiffness increased, highlighting its suitability for long-term durability assessment. SBPS showed the closest agreement between experimental and numerical EMI responses (RMSD = 4.59%), making it the most reliable configuration. NBPS had a higher RMSD (16.5%) but allows sensor reuse and non-invasive deployment. EPS (RMSD = 8.1%) highlights the challenges of modeling multi-layer PZT–epoxy–mortar interactions and interfacial effects. Complementing conventional EMI metrics, equivalent structural parameter (ESP) analysis using real and imaginary impedance components within Hixon's spring–mass–damper framework provided quantitative insight into mechanical evolution during concrete hydration. EPS and SBPS effectively captured stiffness gain and damping reduction, whereas NBPS exhibited more stable yet limited variation. Numerical simulations were performed using COMSOL Multiphysics, enabling detailed modeling of the electromechanical interactions and structural responses across different sensor configurations. By systematically benchmarking sensitivity, reliability, and modeling complexity across configurations, this work delivers critical insights for optimizing EMI-based SHM frameworks. Overall, EPS maximizes sensitivity, SBPS ensures superior numerical–experimental fidelity, and NBPS provides a pragmatic compromise, collectively establishing a robust framework for optimizing EMI-based structural health monitoring in reinforced concrete.

Keywords: *PZT sensor; Electromechanical impedance; Numerical simulation; COMSOL™ 5.5; Structural health monitoring; Equivalent structural parameter*

1. INTRODUCTION

The increasing demand for sustainable and safe infrastructure highlights the need for effective structural health monitoring (SHM) systems to ensure durability and prevent failures. Monitoring compressive strength evolution during curing in concrete structures is critical for assessing load-bearing capacity, enabling predictive maintenance, and enhancing structural reliability [1]. Since many key characteristics of concrete are directly related to compressive strength, evaluating this parameter is crucial for determining the overall quality of the material [2]. Conventional non-destructive methods are thorough but labor-intensive and inconsistent for continuous strength monitoring [3]. This has driven the integration of smart materials like lead zirconate titanate (PZT) into health monitoring systems. PZT, a piezoelectric material widely used in SHM, operates in direct (converting mechanical stress into electrical charge) and converse (generating mechanical strain from an electric field) modes, qualifying it as a smart material [4]. These sensors leverage the electromechanical impedance (EMI) technique, where the interaction between the mechanical properties of the structure and the electrical characteristics of the piezoelectric material

is analyzed. Utilizing this technique, PZT transducers interact with host structures via high-frequency excitations, capturing EMI or impedance signatures that reflect the structure's physical state, enabling precise and continuous monitoring [3].

The use of piezo sensors in SHM extends to various configurations, such as surface-bonded (SBPS), embedded (EPS), and non-bonded piezo sensors (NBPS). SBPS are the most studied configuration due to their direct contact with the host structure and ease of installation [5–8]. SBPS, typically with dimensions of 10 × 10 × 0.2–0.3 mm and sometimes larger (e.g., 20 × 20 × 0.508 mm). Previous studies have employed different frequency intervals ranging from 40 kHz to over 450 kHz, covering both low- and high-frequency responses of concrete structures [9–11]. Lower bands are often selected to capture global stiffness-related changes, while higher bands emphasize localized resonance effects. To ensure that the present simulation encompasses both ends of the spectrum and does not miss critical response features highlighted in earlier works. EMI signatures collected throughout a wide curing period (from 4–8 hours to 365 days) revealed significant deviations in early curing stages (3–5 days), indicating rapid strength development [10,12,13]. Additionally, an exponential increase in frequency shift was observed during the hydration process, correlating with changes in the mechanical properties of concrete [9]. Embedded piezo sensors extend SHM capabilities by integrating directly into the concrete during casting, capturing hydration effects from within the material. Experimental models typically simulate this configuration by embedding a PZT patch within a small mortar specimen, which is then incorporated into the concrete mold prior to casting. The embedded PZT patch effectively monitors the early-stage setting (3–7 days) and transitions to stiff aggregates after 7 days [14,15]. The EMI method is well-suited for tracking curing progression and detecting applied stress [16]. NBPS offer flexibility for temporary monitoring by surface-mounting a PZT patch on aluminum foil, which is then covered with an adhesive layer and attached to the concrete specimen. This configuration, referred to as a smart sensor probe, models the NBPS setup. The flexible and lightweight non-bonded piezo sensor effectively transmits structural vibrations to maintain resonance in high-damping materials like concrete, tracking hydration progress with minimal changes at 3 hours and significant variation at 12 and 24 hours [17]. The Fig. 1 illustrates the schematic diagram of three configurations of PZT used for monitoring the compressive strength of concrete via EMI technology.

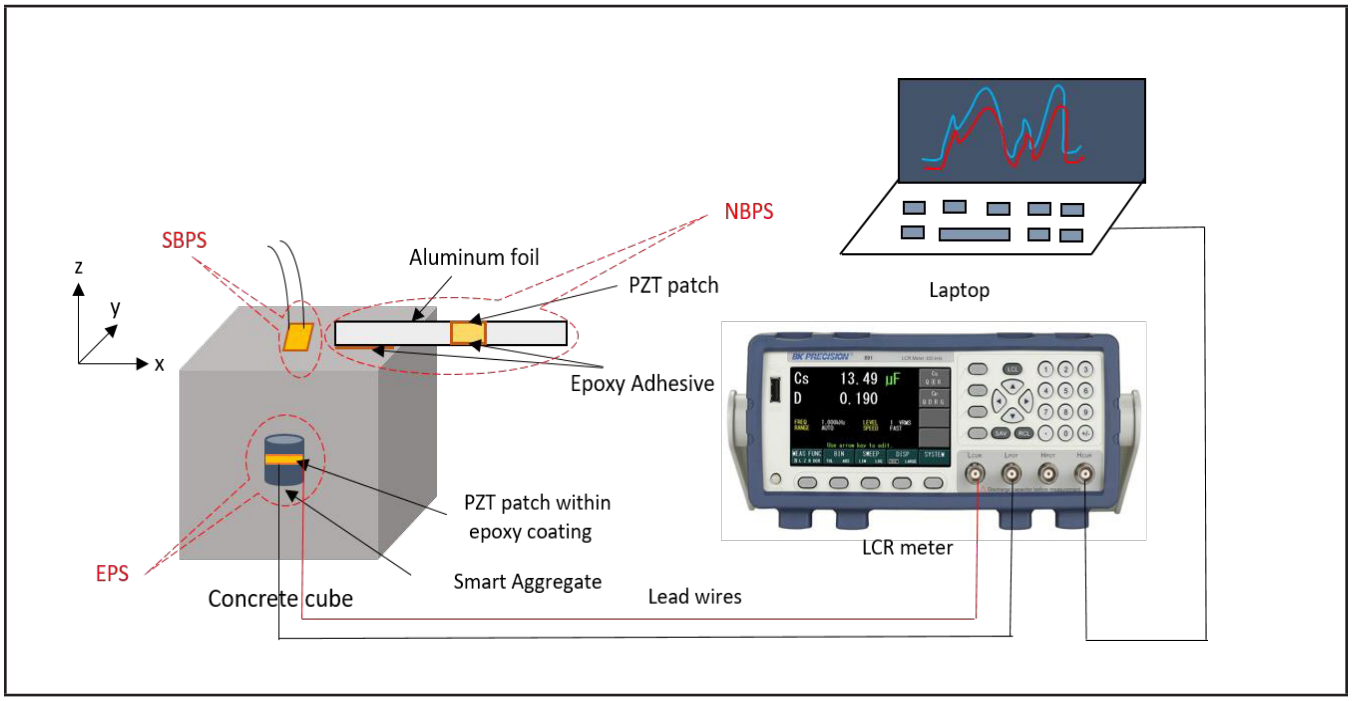

Fig. 1: Schematic diagram of all three piezo configurations with experimental setup

Despite the widespread use of EMI techniques in experimental research, the application of numerical simulations for various sensor configurations, particularly in the context of concrete strength monitoring, remains underexplored, with most studies focusing primarily on experimental setups. Numerical simulations for SBPS and EPS have been investigated in several studies. For instance, Nguyen et al. [18] evaluated the functional performance of piezoelectric-based smart interfaces under various degradation conditions using a COMSOL simulation framework previously developed by Huynh et al. [19]. Bansal et al. [20]conducted numerical simulations to study strength evolution in cement paste embedded with PZT elements during curing. Similarly, Jena et al. [13] investigated the evolution of concrete strength for an SBPS configuration through both experimental and numerical methods. In a subsequent study, Jena et al. [21] advanced this line of research by developing a deep learning–based framework that utilized a non-bonded piezoelectric sensor system for early-age concrete strength monitoring, integrating both experimental investigations and numerical modeling.

Although a number of studies have explored SBPS, EPS, and NBPS configurations individually through experimental or numerical approaches, there is still no systematic investigation that directly compares the performance of all three under a unified framework Addressing this gap is essential, as such a comparative study can provide clear insights into the relative strengths and limitations of each configuration, thereby guiding the optimal selection of piezoelectric sensors for reliable and efficient concrete strength monitoring. To address this gap, the present study employs COMSOL Multiphysics to develop and evaluate numerical models of SBPS, EPS, and NBPS configurations, enabling a systematic comparison of their effectiveness in monitoring concrete compressive strength. Numerical simulations provide a cost-efficient and scalable approach with precise control over boundary and material conditions, thereby allowing direct performance assessment of the three sensor systems without the limitations inherent to experimental testing. Through this framework, the study aims to advance sensor selection strategies for concrete strength monitoring, contributing to more effective and economical SHM practices.

2. FUNDAMENTALS OF EMI TECHNIQUE IN PIEZO SENSOR CONFIGURATIONS

The EMI technique leverages the interaction between mechanical and electrical properties of piezoelectric materials to monitor structural health. EMI uses a PZT patch affixed to the host structure with epoxy adhesive, embedded in, or indirectly coupled to metallic strips or probes as shown in Fig. 2. The experimental procedure for obtaining EMI signatures begins with securely affixing the PZT patch to the specimen. After the patch is attached, lead wires from the PZT patch are connected to an Inductance(L), Capacitance(C) and Resistance(R) meter, which measures the impedance. The LCR meter is then connected to a computer, where the impedance data is recorded and analyzed to obtain the EMI signatures. As the hydration process progresses, the mechanical impedance of the concrete changes, reflecting alterations in its strength and structural integrity. These changes can be detected through the corresponding variations in electrical admittance. The behavior of piezoelectric materials, which can convert mechanical stress into electrical signals and vice versa, can be understood through the following two fundamental equations:

Equation for Electric Displacement (D):

$$D = \overline{\varepsilon^T} E + d^d T \quad (1)$$

Equation for Strain (S):

$$S = d^c E + \overline{S^E} T \quad (2)$$

The first equation shows that electric displacement (charge) is influenced by both mechanical stress (T) and the electric field (E), while the second equation explains how the material's strain (deformation) results from the combination of stress and the electric field. The material's ability to generate electricity and deform under these influences depends on its piezoelectric properties (d) and elasticity (S^E) The superscripts, d and c denote the direct and converse piezoelectric effects. Similarly, the suffixes T and E denote that the quantities are measured under continuous stress and electric field conditions, respectively.

According to Bhalla and Soh [8], the mechanical impedance of the host structure is exactly related to the electrical admittance function ($\bar{Y}$) at a given angular frequency (ω) as in (3).

$$\bar{Y} = G + Bj = 4\omega j \frac{l_p^2}{t_p}\left[\bar{\varepsilon}_{33}^T - \frac{2\,d_{31}^2\,\overline{Y^E}}{(1-\mu_p)} + \frac{2\,d_{31}^2\,\overline{Y^E}}{(1-\mu_p)}\left(\frac{z_{a,e_{ff}}}{z_{s,e_{ff}}+z_{a,e_{ff}}}\right)\left(\frac{\tan(kl_p)}{(kl_p)}\right)\right] \quad (3)$$

where is given by conductance (G) and susceptance (B). These terms are influenced by the mechanical properties of the piezoelectric sensor and the structure it is attached to. In the last term, $Z_{a,e_{ff}}$ is the mechanical impedance of the PZT patch itself $Z_{s,e_{ff}}$ and is the mechanical impedance of the structure, both being measured separately. denotes half the length, t_p refers to the thickness of the patch, l_p and d_{31} is the deformation sensitivity coefficient of piezoelectric materials, showing how the material responds to applied stress. $\bar{\varepsilon}_{33}$ is the PZT patch's complex electric permittivity at zero stress, indicating its ability to store charge. The complex modulus of elasticity is denoted by $\overline{Y^E}$, k represents the wavenumber, μ_p is the Poisson's ratio, which describes how the material deforms in the lateral direction when stretched or compressed.

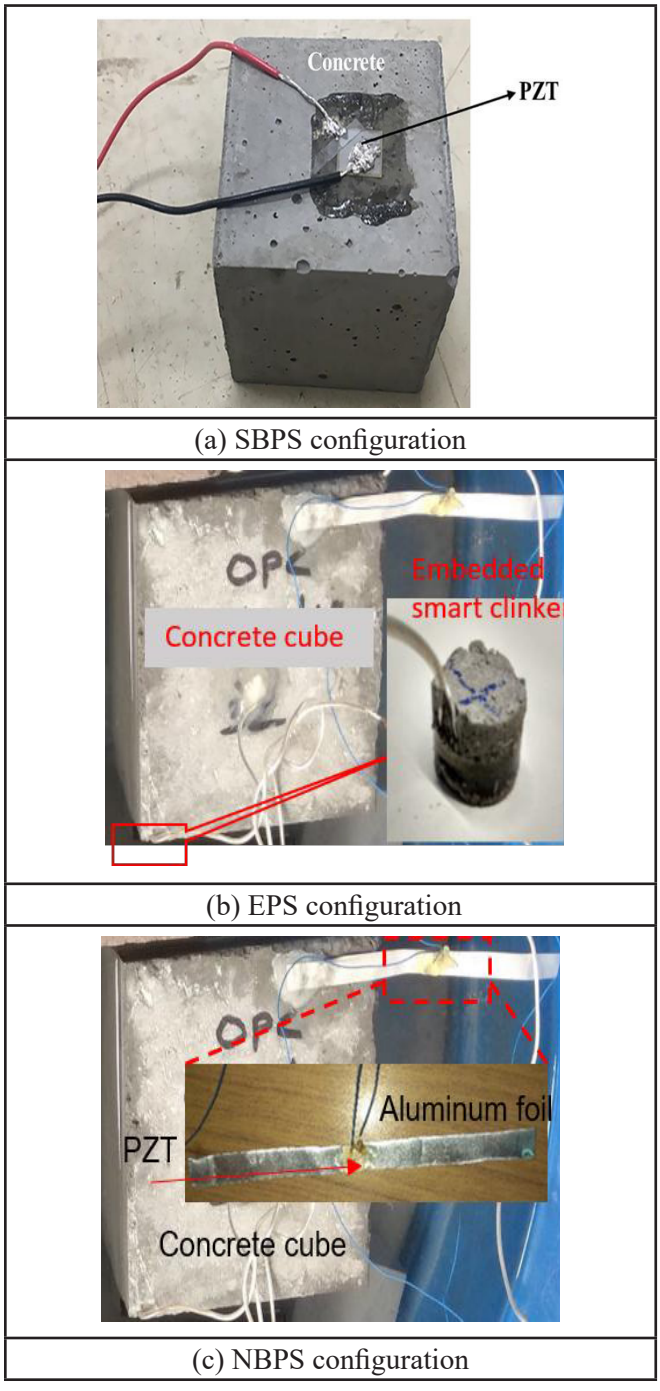

(a) SBPS configuration

(b) EPS configuration

(c) NBPS configuration

Fig. 2: Different Piezo configuration

The impedance-based method operates within 30–400 kHz for optimal detection [22]. Higher frequencies (above 200 kHz) are useful for locating defects, while lower frequencies (below 70 kHz) cover a wider area [23]. Frequencies over 500 kHz are less effective. PZT patches (5–15 mm in size, 0.1–0.3 mm thick) function efficiently in this range, providing reliable results for detecting small mechanical or physical changes [24]. The present study was conducted within the frequency range of 30–300 kHz, with measurements taken at 100 Hz intervals. According to an experimental study [25], it was observed that beyond 300 kHz, the changes in the system are minimal.

2.1 Equivalent Structural Parameter (ESP) Concept

In EMI studies, many investigations have focused only on direct changes in the conductance spectra, using simple statistical indicators such as mean squared error (MSE) or root mean squared error (RMSE) to track damage. Although these indices are easy to apply, they often provide only a superficial assessment and fail to reveal how the actual mechanical properties of the structure evolve. To gain a more precise understanding of structural behavior, it is essential to extract the effective structural and mechanical impedance at the sensor interface from the raw EMI response. This requirement forms the basis for adopting a more detailed analytical approach.

To achieve a more detailed understanding of structural behavior, it is necessary to extract the effective structural and mechanical impedance of the concrete–sensor system from the EMI response. This procedure is referred to as the ESP method. Bhalla and co-workers [26] first demonstrated that EMI signatures could be quantitatively associated with physical parameters such as stiffness (k), damping (c), and mass (m), particularly

in the context of concrete hydration. The underlying formulation as in Equations (4–6) separates the overall impedance expression into two components: a passive component, governed solely by the intrinsic properties of the piezoelectric transducer, and an active component, which reflects the combined interaction between the transducer and the host structure. This distinction arises because the terms $Z_{a,e_{ff}}$ and $Z_{s,e_{ff}}$ appear exclusively in the active component.

By analyzing the conductance and susceptance responses, the effective structural impedance, $Z_{s,e_{ff}} = x + yj$ can be separated into its real (x) and imaginary (y) parts, each containing valuable information about the mechanical response of the host material as it undergoes property changes. This methodology has been widely adopted in prior studies [27–31]. To monitor variations in structural characteristics, the real and imaginary components are extracted for each test condition and plotted against frequency. Subsequently, the experimental impedance trends are compared with the equivalent system proposed by Hixon (1998) [32]. Within selected frequency bands, the trends in x and y are matched to an idealized spring–damper representation, enabling the estimation of k and c parameters that replicate the observed structural behavior.

$$\overline{Y} = \overline{Y}_{Passive} + \overline{Y}_{Active} \tag{4}$$

$$\bar{Y}_{Passive} = 4\omega j \frac{l_p^2}{t_p}\left[\bar{\varepsilon}_{33}^{T} - \frac{2\,d_{31}^2 \overline{Y^E}}{(1-\mu_p)}\right] \tag{5}$$

$$\bar{Y}_{Active} = \frac{8\omega\, d_{31}^2 \overline{Y^E} l_p^2}{(1-\mu_p)}\left(\frac{z_{a,e_{ff}}}{z_{s,e_{ff}} + z_{a,e_{ff}}}\right)\left(\frac{\tan(kl_p)}{(kl_p)}\right) j \tag{6}$$

3. EXPERIMENTAL SET-UP OF PIEZO CONFIGURATIONS

The SBPS was installed by attaching a 10×10×0.2mm PZT patch to a 150×150×150 mm concrete cube using 43-grade OPC (IS 8112). Prior to bonding, the specimen surface was cleaned with sandpaper, after which the patch was fixed with adhesive and cured for about 10 minutes at room temperature (Fig. 2a). Electrodes were soldered to the patch, and a protective epoxy coating was applied to minimize environmental effects. This configuration is simple to implement and safe to apply after demolding, though it cannot capture data during the early hydration stage. In contrast, the EPS configuration was realized by fabricating a "smart clinker" (SC), where the PZT patch was sandwiched between two 1-mm epoxy layers resulting in overall dimensions of 11 × 11 × 2.2 mm. This assembly was then encapsulated with two 4-mm mortar layers, producing a cylindrical element of 10.2 mm height and 15 mm diameter. During casting of the concrete cube (150 mm), the SC was positioned at the center, with its lead wires extended outside for subsequent EMI measurements (Fig. 2b).

For the NBPS, the PZT patch was mounted at the center of a thin aluminum foil strip (100x10x1 mm). The patch was fixed with epoxy adhesive and subsequently covered with an additional adhesive layer for protection. During casting, one end of the foil (approximately 25 mm extended) was secured to the concrete cube, leaving the sensor free of direct embedment (Fig. 2c). This arrangement improves sensitivity to minor mechanical disturbances and facilitates efficient transfer of vibrations in concrete, which is typically a high-damping medium. Moreover, the detachable foil interface allows reusability, while its compact and flexible design makes NBPS particularly suitable for deployment in structural elements with complex geometries where SBPS or EPS installation is less feasible. Then EMI measurements were carried out by exciting the transducer with 1 V and recording the baseline electromechanical response using an E4980A Precision LCR Meter (20 Hz–2 MHz). The conductance (G–f) and susceptance (B–f) signatures were obtained in the 30–300 kHz range. After initial measurements, the specimens were water-cured, and EMI data were collected periodically during hydration.

4. NUMERICAL MODELLING

A numerical investigation was conducted using COMSOL Multiphysics to determine concrete compressive strength through EMI signatures from piezoelectric sensors in SBPS, EPS, and NBPS configurations. The study involved several steps: (i) Geometry: Concrete cube, PZT patch, and Epoxy adhesive were created to represent the physical system. (ii) Material: Materials for different elements were assigned based on their physical and electrical properties including mechanical and piezoelectric constants. (iii) Solid mechanics module: This was used to model piezoelectric coupling and analyze mechanical deformations. (iv) Electrostatics module: An electric potential of 1 V is applied to the upper face of the PZT transducer, grounding the lower face to capture the piezoelectric effect. (v) Multiphysics (Piezoelectric Effect): The piezoelectric effect was modeled by coupling the mechanical deformation with

the electrical behavior of the PZT material. (vi) Meshing: A mesh was generated, with finer elements around critical areas like the PZT-concrete interface, ensuring accuracy and efficiency. (vii) Frequency domain study: The EMI response was simulated using a PZT-5A transducer. Its material properties illustrated in Table 1, specified by the manufacturer and experimentally studied by the authors in [23], incorporated into the model to simulate EMI responses. The mechanical properties of PZT include a thickness of 0.2 mm, a Poisson's ratio (μ_p) of 0.4, and a density (ρ) of 7400 kg/m³. Additionally, the damping ratio (ζ) is measured at 0.012, and the dielectric loss factor (δ) is considered as 0.0169, indicating the material's ability to dissipate energy under oscillatory conditions. The material properties of the epoxy layer, mortar, and concrete are illustrated in Table 2.

Table 1: Material properties of PZT [23]

Parameters	Quantities
Elasticity tensor [Pa]	$\begin{bmatrix} 1.272\times10^{11} & 8.02\times10^{10} & 8.47\times10^{10} & 0 & 0 & 0 \\ 8.02\times10^{10} & 1.272\times10^{11} & 8.47\times10^{10} & 0 & 0 & 0 \\ 8.47\times10^{10} & 8.47\times10^{10} & 1.174\times10^{11} & 0 & 0 & 0 \\ 0 & 0 & 0 & 2.30\times10^{10} & 0 & 0 \\ 0 & 0 & 0 & 0 & 2.30\times10^{10} & 0 \\ 0 & 0 & 0 & 0 & 0 & 2.30\times10^{10} \end{bmatrix}$
Relative permittivity	3130
Piezoelectric Constant [C/N]	$\begin{bmatrix} 0 & 0 & 0 & 0 & 7.41\times10^{-10} & 0 \\ 0 & 0 & 0 & 7.41\times10^{-10} & 0 & 0 \\ -2.74\times10^{-10} & -2.74\times10^{-10} & 5.93\times10^{-10} & 0 & 0 & 0 \end{bmatrix}$

Table 2: Material properties of epoxy, mortar, and concrete [23]

Parameters	Quantities		
	Concrete	Mortar	Epoxy
Density	2300	2160	1200
Poisson's ratio	0.2	0.187	0.4
Modulus of elasticity	25	2.87	2

4.1 Unconstrained PZT and PZT with epoxy coating

The PZT element (10x10x0.2 mm) is coated with two 1 mm layers of epoxy, resulting in a total size of 11x11x2.2 mm, as shown in Fig. 3. Conductance and susceptance characteristics were recorded from 30–300 kHz at 100 Hz intervals. The EMI signatures of free and epoxy-coated PZT were plotted (Fig. 4), revealing a decrease in the resonance peak and a shift to a lower frequency. The shift is attributed to the added mass and stiffness of the epoxy coating, which dampens the PZT vibrations and increases the system's stiffness, thereby lowering the resonance frequency, consistent with similar studies [13, 23].

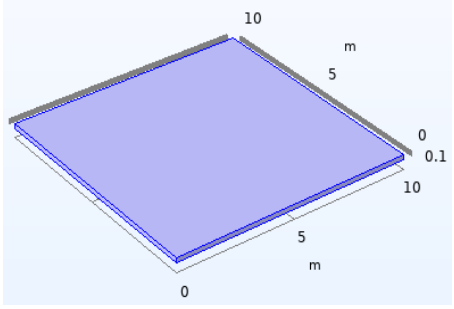

(a) Unrestrained PZT patch

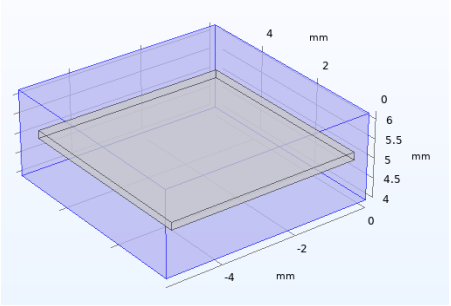

(b)Epoxy-coated PZT

Fig. 3: Three-dimensional model depictions

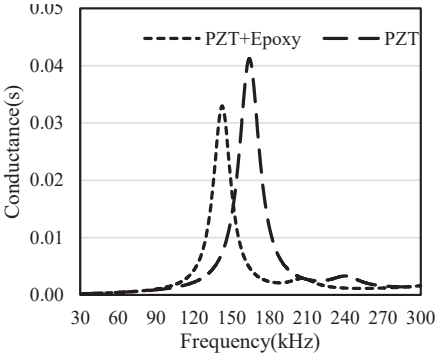

(a) Conductance Signature

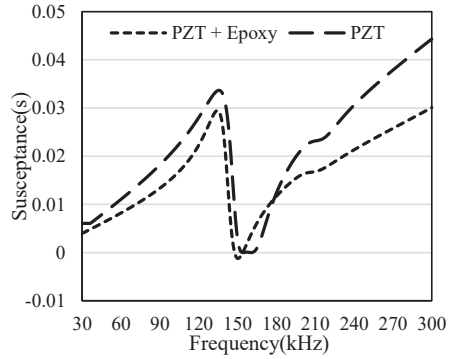

(b) Susceptance signature

Fig. 4: EMI signature plots of unrestrained PZT and epoxy-coated PZT

4.2 Surface-bonded piezo configuration

A 3D model of a surface-bonded PZT sensor (10 mm x 10 mm x 0.2 mm) with 0.5 mm epoxy coatings was attached to a 150 mm^3 cube of concrete (Figure 5a). Material properties, as detailed in Tables 1 and 2, were assigned accordingly. To simulate the realistic setup, a fixed boundary condition on the bottom face of the concrete cube simulated the transducer's physical attachment. A free tetrahedral mesh was employed with a maximum element size of 15 mm and a minimum of 0.3 mm. A quarter-scale model was employed to reduce the computational cost while maintaining the physical fidelity of the system (Fig. 5b). The meshed model comprised 26,553 elements, including 20,314 tetrahedral, 5,786 triangular, 430 edges, and 23 vertex elements, with a refined mesh around the PZT and adhesive regions, as shown in Fig. 5(c), to capture localized responses accurately. Conductance and susceptance characteristics were recorded from 30–300 kHz at 100 Hz intervals.

Figure 6(a) and (b) presents the validation plots for 30 MPa, comparing experimental results [11] with the numerical conductance data. The curves demonstrate a strong match, with only minor deviations. These discrepancies are likely due to small variations in experimental conditions and slight inaccuracies in the input material properties used in the simulations. With the numerical model successfully validated against experimental results, further numerical simulations were conducted to analyze the EMI signatures corresponding to varying concrete strengths. Fig. 6(b) shows the conductance-frequency responses for varying concrete strengths, represented by changes in Young's modulus. As Young's modulus increases with hydration, the curve shifts upward to the right, indicating higher resonant frequencies and conductance values, reflecting increased concrete stiffness over time.

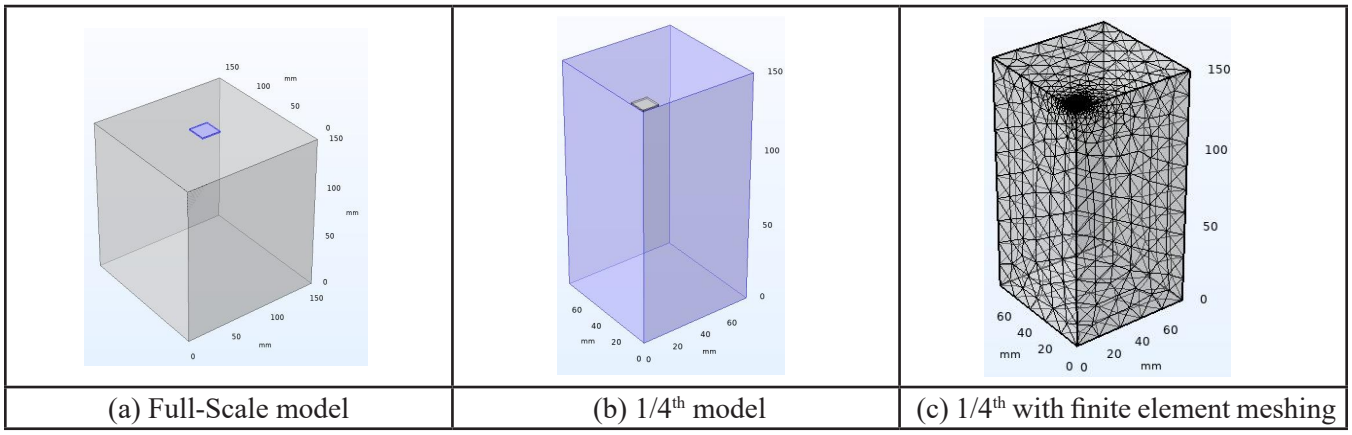

Fig. 5: Concrete specimen with SBPS

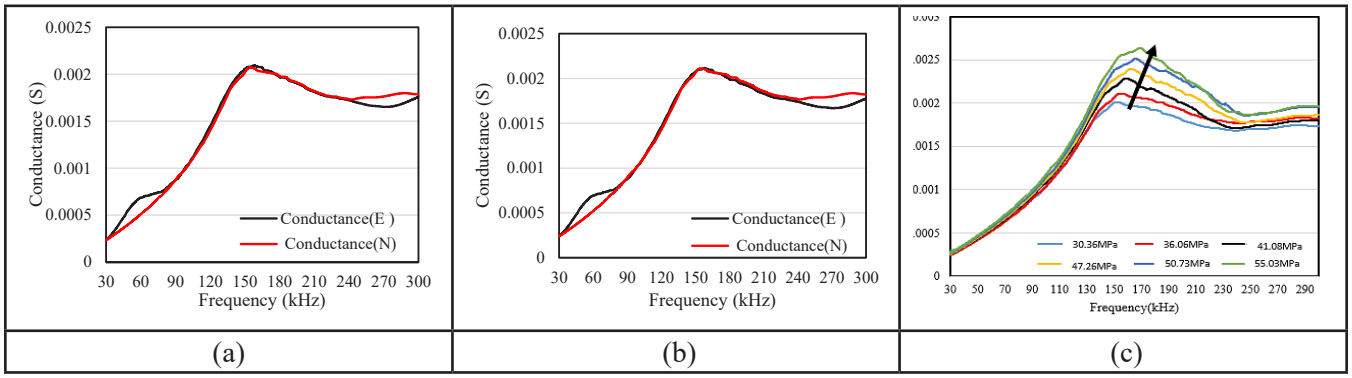

Fig. 6: Validation plot of experimental and numerical conductance for SBPS configuration (a) 30.36MPa concrete (b) 36.06MPa concrete (c) Numerical simulation plot for various concrete strengths

4.3 Embedded piezo configuration

In line with the experimental setup described earlier, the SC configuration was replicated in COMSOL by modeling the PZT patch, epoxy layers, and surrounding mortar as detailed in Section 3. This ensured consistency between the experimental realization and the numerical simulation. Figures 7(a), (b), and (c) illustrate the SC, full-scale, and quarter-scale cube models, respectively. The model was meshed using a free tetrahedral approach, similar to the SBPS model. A finer mesh was applied to the PZT and adhesive regions to enhance accuracy while maintaining consistent maximum and minimum element sizes. The final mesh, as shown in Fig. 7(d), consisted of 20,365 elements, including 17,151 tetrahedral, 2,853 triangular, 327 edge, and 34 vertex elements. Fig. 8(a) and (b) illustrate the validation result by comparing experimental conductance data with the corresponding numerical results for 30.36 MPa and 36.06 MPa. A close agreement between the two curves is observed, with only minor deviations. Fig. 8(c) illustrates the numerical simulation outcomes showing the conductance-frequency relationship for various concrete strength levels.

The plot analysis highlights a positive correlation between curing time and the growth of Young's modulus, reflecting the hydration process. The zoomed view reveals that the upward trend in resonance peaks with curing time indicates reduced concrete resistance and enhanced conductivity. These findings corroborate the trends predicted by the proposed EMI model [23].

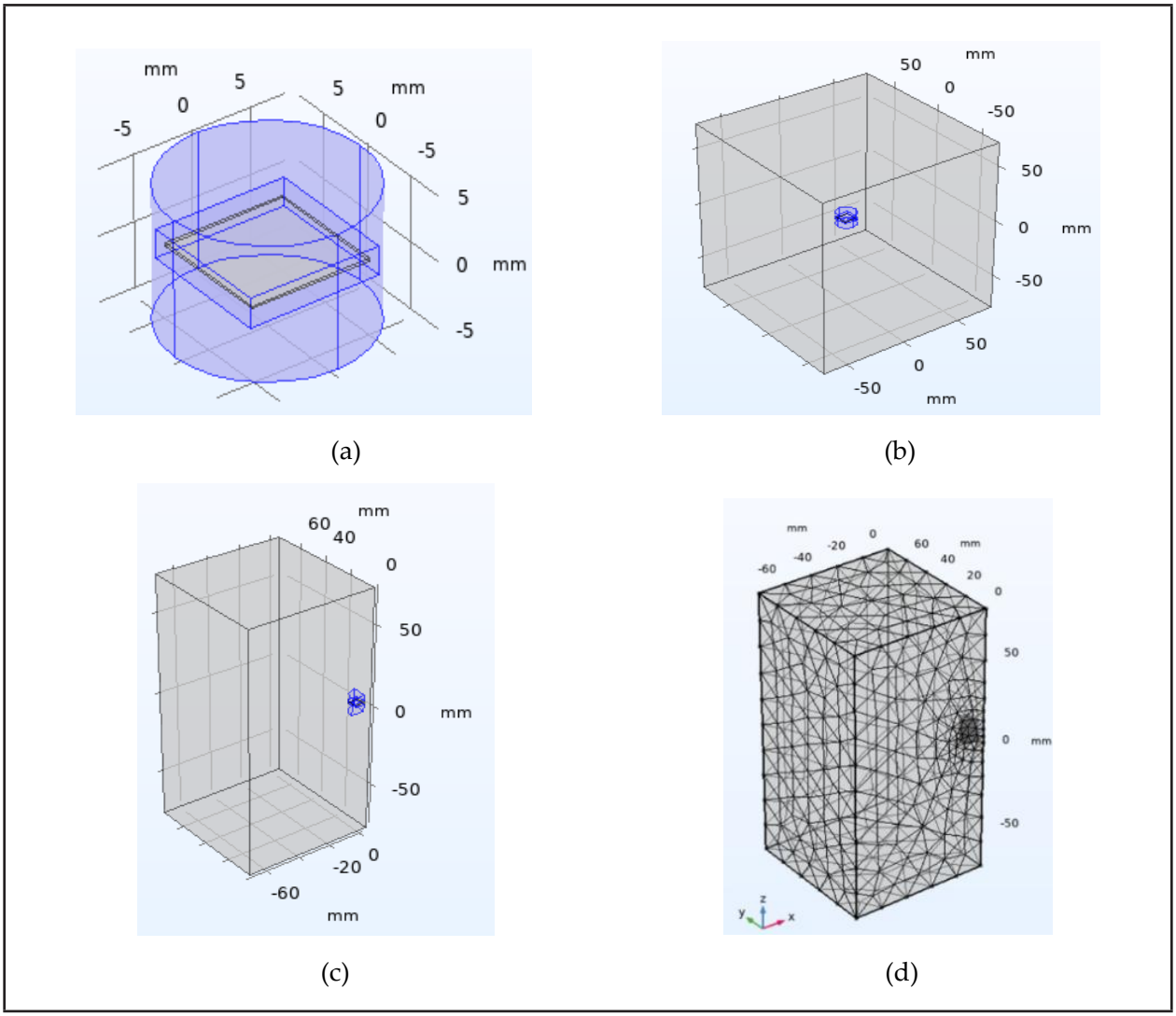

Fig. 7: 3D representation of (a) Smart clinker, (b) Full-scale model, (c) Quarter-scale model, and (d) Quarter-scale model with finite element meshing

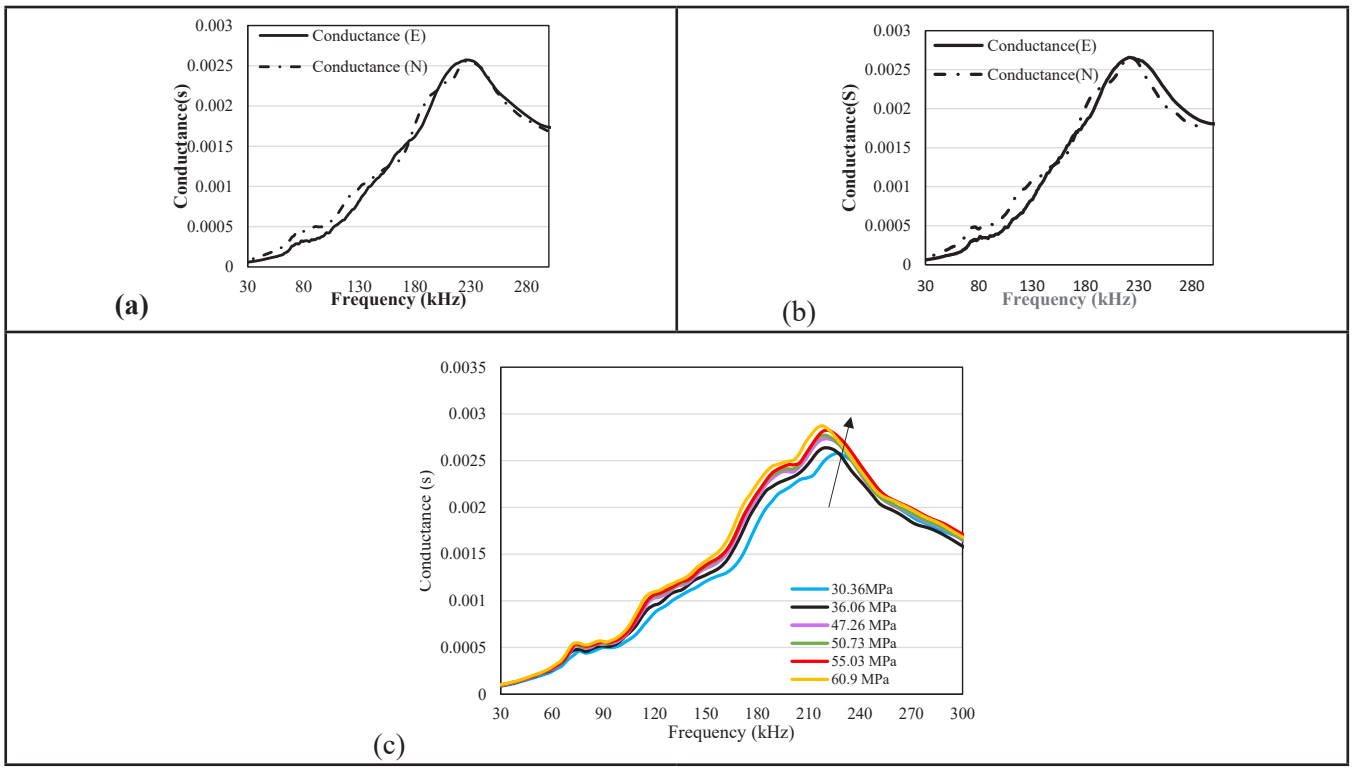

Fig. 8: Validation plot of experimental and numerical conductance for EPS configuration (a) 30.36MPa concrete (b) 36.06MPa concrete (c) Numerical simulation plot for various concrete strength

4.4 Non-bonded piezo configuration

Figure 9(a) illustrates the configuration of the smart sensor probe. The PZT element was centrally mounted on a 100 mm × 10 × 1 mm² aluminum foil segment with adhesive, followed by an additional adhesive layer for encapsulation during casting. The foil's extended end (25 mm) was affixed to the concrete specimen, as depicted in Fig. 2, while Fig. 9(b) presents a probe adhered to a concrete cube using epoxy. Fig. 9(c) presents the NBPS configuration with finer finite element meshing. A free tetrahedral meshing technique was employed in the 3D model, generating 57,458 elements with adaptive refinement near boundaries and element sizes from 0.9 mm to 12.4 mm to ensure accuracy for complex geometries. Numerical simulations were conducted over a 30–300 kHz frequency range with 100 Hz increments. The foil significantly improves sensitivity by transmitting vibrations efficiently, even in high-damping media like concrete, ensuring resonance detection. Its reusability and adaptability make it suitable for complex structural configurations, such as bridge joints and intricate geometries, where traditional bonded setups like SBPS and EPS face limitations.

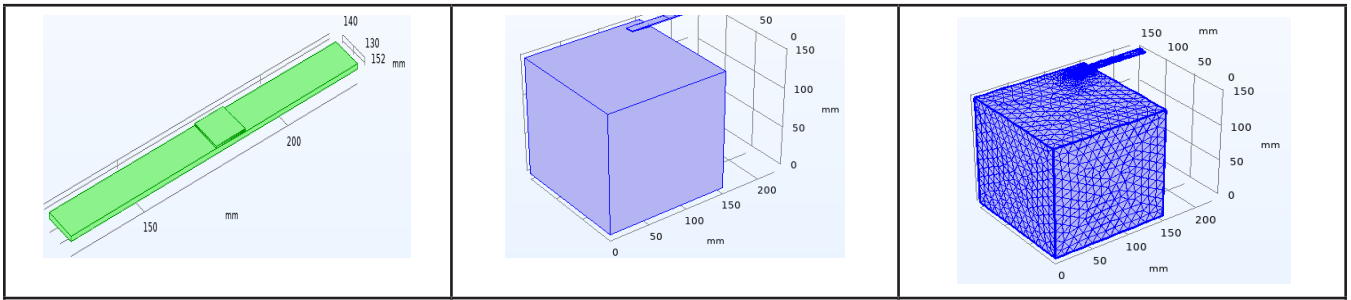

(a) Smart sensor prob	(b) NBPS configuration	(c) NBPS with Finite element meshing

Fig, 9: 3D representation NBPS configuration affixed to specimen

Figure 10(a) and (b) present the validation of the NBPS model against experimental results for 30.36 MPa and 36.06 MPa, showing reasonable agreement with minor deviations. Fig. 10(c) extends the comparison across different strength levels. The results indicate that with increasing strength, the conductance peak generally rises, reflecting improved rigidity and sensor response. However, due to the presence of the aluminum foil interface in the NBPS system, the sensor–concrete interaction is less direct than in bonded configurations. This reduced coupling leads to comparatively smaller variations and overlapping trends in the conductance curves. Consequently, the resonance shifts and conductance changes are subtler, demonstrating that while NBPS offers practical advantages such as reusability and ease of installation, it exhibits lower sensitivity to material property changes compared to SBPS and EPS setups.

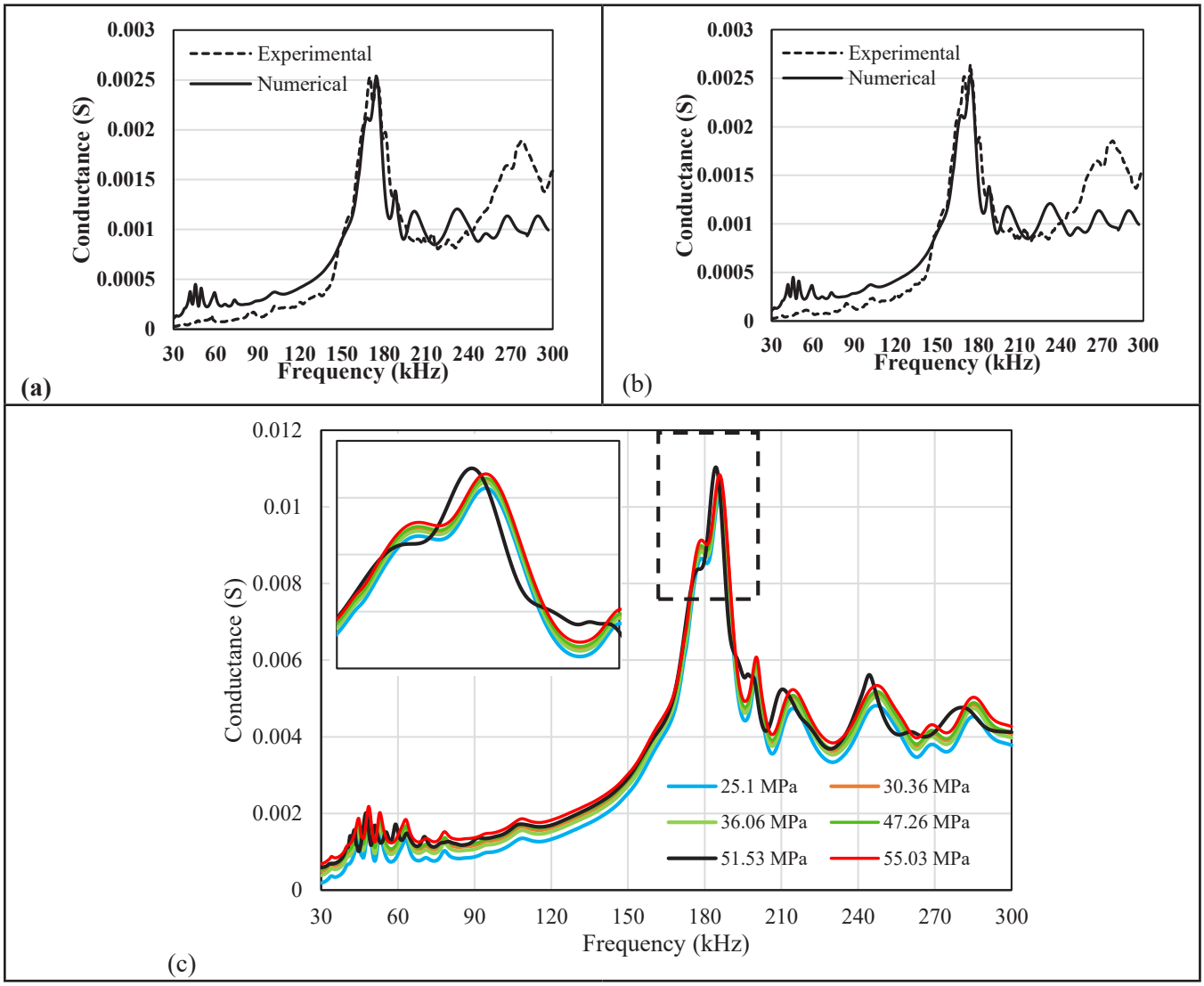

Fig. 10: Validation plot of experimental and numerical conductance for NBPS configuration (a) 30.36MPa concrete (b) 36.06MPa concrete (c) Numerical simulation plot for various concrete strengths

5. ANALYSIS AND RESULT

5.1 Qualitative Analysis of Conductance–Frequency Response

The analysis of conductance vs. frequency curves in Fig. 11 for SBPS, EPS, and NBPS reveals that as concrete strength increases, both the conductance resonance peak (CRP) and resonance frequency (CRF) rise, reflecting enhanced rigidity and sensor response. The SBPS configuration shows a maximum conductance of 0.0025–0.0027 with a resonance peak in the 150-170 kHz range. The EPS configuration performs better, with a conductance of 0.003 and a resonance peak at 220-240 kHz, making it highly effective for long-term maintenance and monitoring of concrete structures. In contrast, the NBPS configuration exhibits lower conductance (0.0025–0.0027) and a resonance peak in the 180-190 kHz range. The upward and rightward trend in the conductance vs frequency curve across all configurations shows that as concrete strength increases, both conductance and resonance frequency rise. Among the configurations, EPS offers the highest sensitivity, making it ideal for long-term maintenance and monitoring of concrete structures ensuring proactive structural health management in real-world applications.

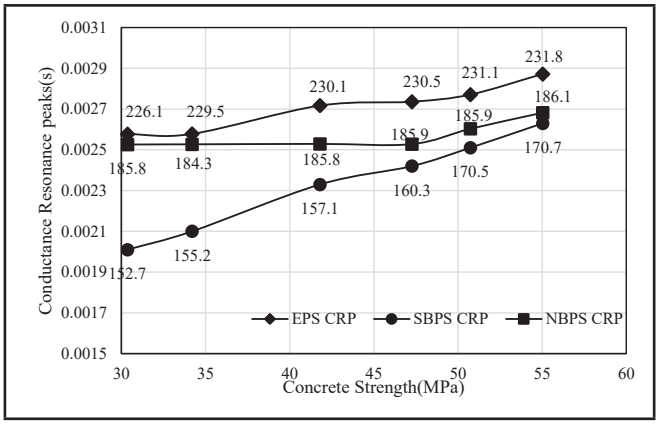

Fig. 11: Variation of conductance resonance peaks (CRP) with concrete strength for different sensor configurations (SBPS, EPS, and NBPS).

5.2 Quantitative Assessment

To complement the qualitative comparison of EMI signatures, a quantitative evaluation was performed using the Root Mean Square Deviation (RMSD), which is widely employed in EMI-based SHM studies. RMSD quantifies the overall discrepancy in impedance response between experimental and numerical models, thereby reflecting how well the model captures electromechanical coupling effects. It is defined as:

$$RMSD = \sqrt{\frac{\sum_{i=1}^{N}\left(G_i^{exp} - G_i^{num}\right)^2}{\sum_{i=1}^{N}\left(G_i^{exp}\right)^2}} \quad (7)$$

where G_i^{exp} and G_i^{num} represent the experimental and numerical conductance values at the i^{th} frequency point, and N is the total number of frequency points. The normalization with respect to the squared experimental response renders the index dimensionless, allowing consistent comparison across sensor configurations.

The computed RMSD values for the SBPS, EPS, and NBPS configurations were 4.59%, 8.10%, and 16.5%, respectively (Figure 12). These results, obtained by comparing the numerical model directly with experimental signatures, are reported for the 30.36MPa (5 days) case; similar magnitudes and the same ranking of sensor configurations were observed at other strength levels, indicating a consistent trend. The EPS configuration shows moderate deviation, attributed to the multilayered PZT–epoxy–mortar assembly where multiple interfaces and boundary conditions introduce discrepancies in stress transfer and damping. The NBPS configuration exhibits the largest deviation, but it offers the advantage of reusability, making it a practical trade-off between accuracy and operational flexibility. Overall, the RMSD analysis demonstrates that SBPS achieves the most accurate experimental–numerical match, EPS retains acceptable accuracy despite interface complexities, and NBPS balances accuracy with ease of reuse.

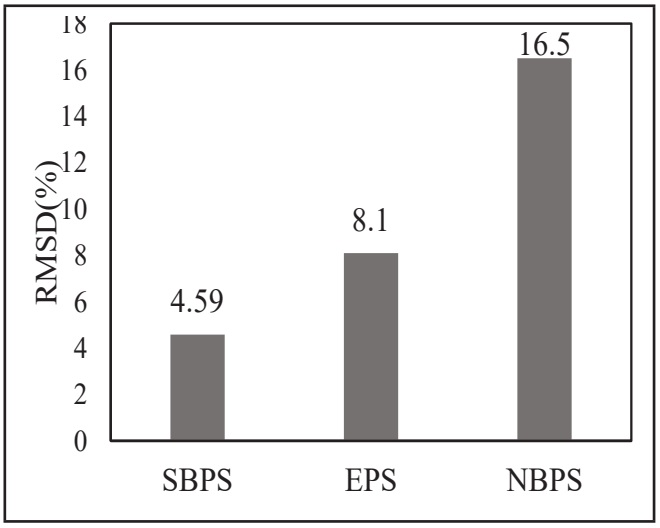

Fig. 12: RMSD comparison plot for different sensor configurations

5.3 ESP Analysis of Sensor Configurations

Figures 12–14 present the results of the ESP analysis for the three sensor configurations: EPS, NBPS, and SBPS. Figure 13 compares the real (x) and imaginary (y) components of the numerically extracted mechanical impedance with the equivalent system response across the selected frequency range. In all three cases, the equivalent system demonstrates close correspondence with the numerical system, indicating that the underlying behavior can be reliably represented using an equivalent model.

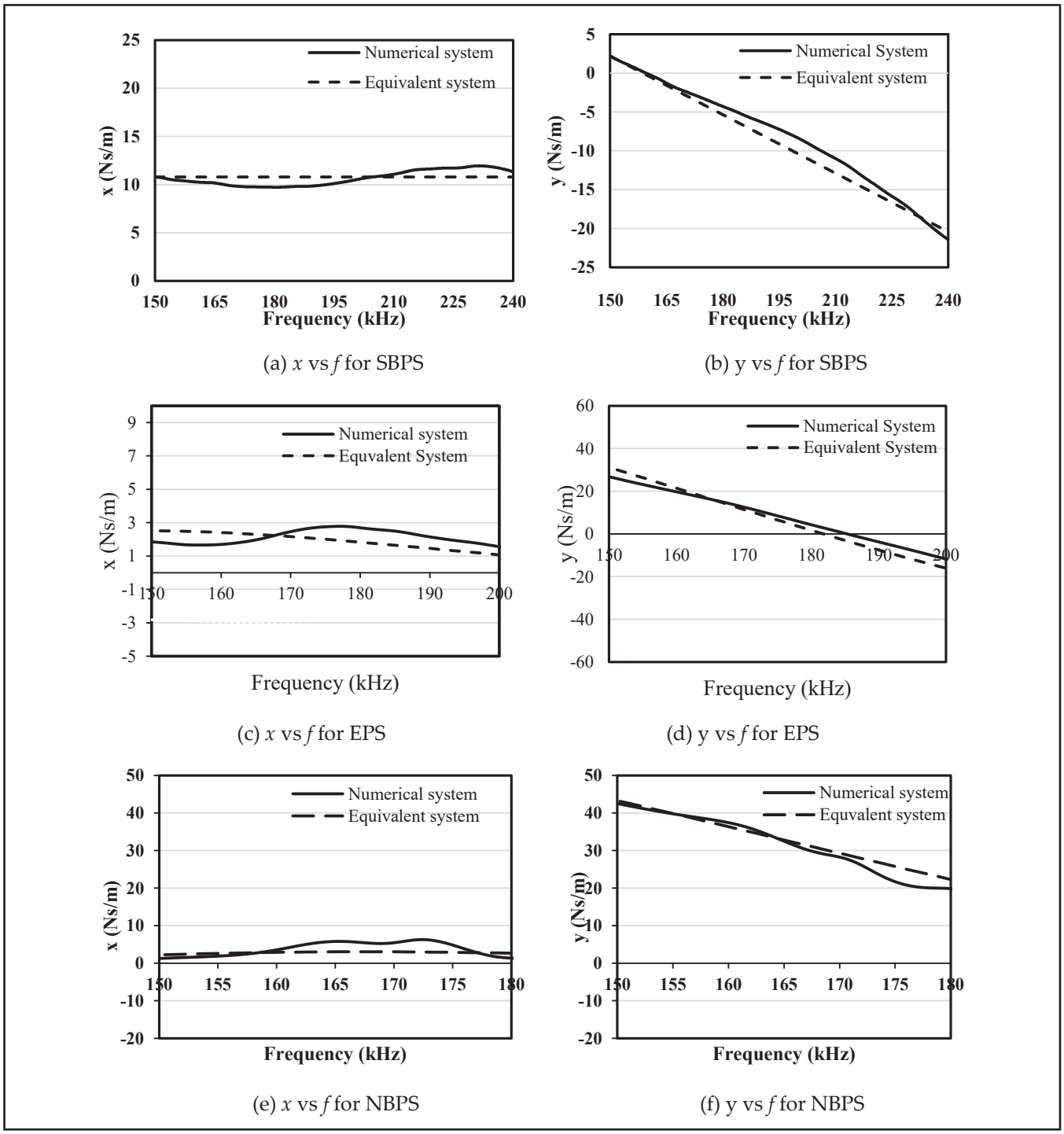

Fig. 13: Real and imaginary impedance components for different sensor configurations.

Figure 14 illustrates the spring–mass–damper model proposed by Hixon, along with the corresponding impedance plots. The results confirm that for all configurations, the system response aligns well with Model 7 of Hixon's study, validating the use of the mass–spring–damper framework for characterizing the interaction between the PZT sensor and the host concrete. The comparative analysis of SBPS, EPS, and NBPS configurations in Fig. 15 highlights the influence of sensor–concrete interaction on stiffness (k) and damping (c) evolution during curing. SBPS showed a marked rise in stiffness (~50–55 kNs/m by 28 days) and a sharp reduction in damping (~130–140 Ns/m), indicating high sensitivity to strength gain. EPS exhibited a similar but more gradual trend, with k increasing from 30.28 to 57.63 kNs/m and c decreasing from 112.36 to 51.75 Ns/m between day 1 and 90, with most changes occurring within 28 days. In contrast, NBPS showed minimal variation, with stiffness stabilizing near 30.48 kNs/m and damping decreasing slightly (~406.5 to 397 Ns/m). The limited sensitivity of NBPS is attributed to its non-bonded interface, which reduces coupling but offers a non-invasive monitoring option. Overall, SBPS and EPS provide strong sensitivity to hydration-induced property changes, while NBPS prioritizes practicality over resolution.

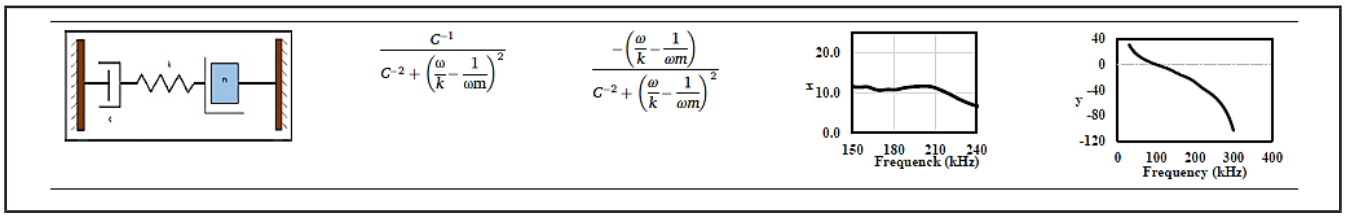

Fig. 14: Equivalent spring–mass–damper model with governing equations and impedance response (x and y)

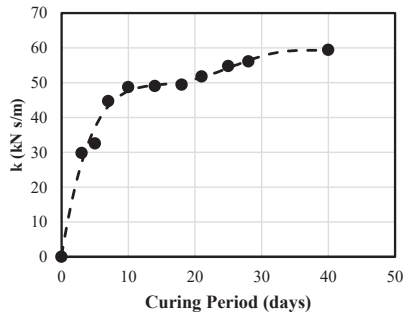

(a) Equivalent Stiffness vs days for SBPS

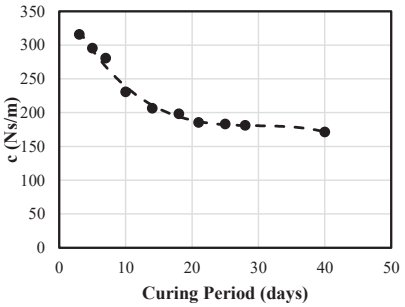

(b) Damping vs days for SBPS

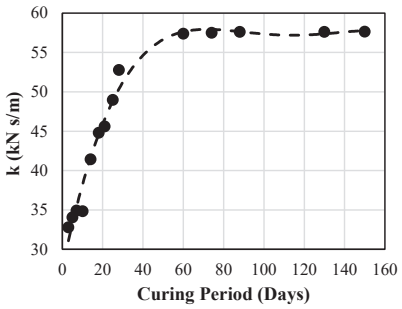

(c) Equivalent Stiffness vs days for EPS

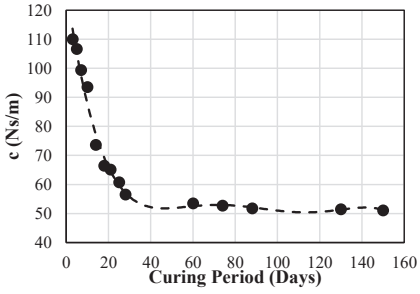

(d) Damping vs days for EPS

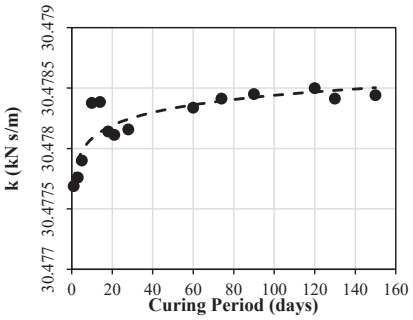

(e) Equivalent Stiffness vs days for NBPS

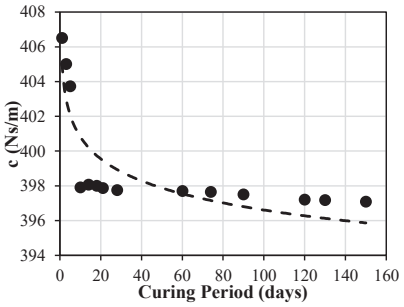

(f) Damping vs days for NBPS

Fig. 15: Evolution of equivalent structural parameters (k and c) during curing for different sensor configurations

To provide a comprehensive assessment, a representative Fig. combining both experimental and numerical data of SBPS configuration is presented in Fig. 16. This allows a direct comparison and validation of the numerical model against measured responses, thereby clarifying the accuracy of the predictions and supporting the observed trends in stiffness (*k*). It is evident that the stiffness of the specimens increases with curing days, as reflected in both experimental and numerical data, which is consistent with the expected evolution of concrete mechanical properties. Both curves show a similar trend: a rapid initial increase followed by a gradual plateau, indicating progressive stiffness development over time. A consistent offset is observed, with numerical predictions underestimating the experimental response, likely due to simplified boundary conditions and homogenized material properties. Nonetheless, the model accurately captures the overall trend, confirming its suitability for assessing stiffness evolution and comparing sensor configurations. For reference, similar figures for the EPS and NBPS configurations exhibit the same trend, demonstrating consistent model performance across all sensor setups.

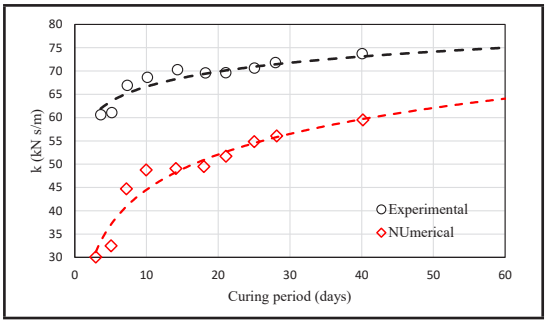

Fig. 16: Comparison of Experimental and Numerical ESP Responses for SBPS Configurations

6. CONCLUSION

This study systematically evaluated three sensor configurations, SBPS, EPS, and NBPS, for monitoring concrete strength evolution using the EMI technique, supported by both experimental measurements and finite element simulations using COMSOL Multiphysics. The comparative analysis of conductance–frequency signatures revealed a consistent upward and rightward shift in resonance peaks with increasing concrete strength, signifying enhanced stiffness and improved sensor response across all configurations. Among the investigated systems, the EPS configuration exhibited the highest sensitivity, with pronounced resonance peaks in the 220–240 kHz range, making it particularly suitable for long-term durability monitoring. In contrast, the SBPS configuration, though associated with lower peak conductance, achieved the closest match between experimental and numerical results, as demonstrated by its lowest NRMSD value (3.96%), thereby underscoring its superior reliability in replicating EMI responses. The NBPS configuration, characterized by the presence of an aluminum foil layer, offered a balance between accuracy and practicality, showing moderate agreement with experimental data while retaining the advantages of reusability and ease of deployment. The quantitative assessment through RMSD and NRMSD metrics confirmed that modeling complexity plays a critical role in simulation accuracy. The comparatively higher NRMSD for the EPS configuration (25.65%) was attributed to its multi-layered composite structure (PZT–epoxy–mortar), which introduces additional interfacial interactions that are difficult to replicate precisely in numerical models. This highlights the importance of carefully addressing material heterogeneity, damping, and bonding conditions in future modeling efforts.

Furthermore, the ESP analysis provided deeper insights into the mechanical evolution of concrete during hydration. Across all three configurations, the extracted real and imaginary impedance components aligned with Model 7 of Hixon's framework, validating the applicability of a spring–mass–damper analogy. The results revealed that EPS and SBPS effectively captured stiffness gain and damping reduction during curing, whereas NBPS exhibited comparatively limited variation, attributable to its non-bonded interface. Nonetheless, NBPS demonstrated stable responses and retained its advantage as a non-invasive, reusable sensing option. Overall, the findings establish that while EPS offers superior sensitivity and is best suited for long-term durability monitoring, SBPS ensures the highest numerical–experimental consistency, and NBPS provides a practical compromise between accuracy and reusability. Integrating ESP with conventional EMI metrics enhances the interpretability of sensor responses and lays a stronger foundation for optimizing EMI-based SHM frameworks in reinforced concrete infrastructure.

FUNDING

The corresponding author of this article gratefully acknowledges support from the Science and Engineering Research Board (SERB), Department of Science and Technology, Government of India, under grant SRG/2023/000306.

REFERENCES

[1] Gu H, Song G, Dhonde H, Mo YL, Yan S. Concrete early-age strength monitoring using embedded piezoelectric transducers. Smart Mater Struct 2006;15:1837–45. https://doi.org/10.1088/0964-1726/15/6/038.

[2] Stephen Pessiki, Matthew R. Johnson. Nondestructive Evaluation of Early-Age Concrete Strength in Plate Structures by the Impact-Echo Method. ACI Mater J 1996;93. https://doi.org/10.14359/9811.

[3] Liang C, Sun FP, Rogers CA. Coupled Electro-Mechanical Analysis of Adaptive Material Systems — Determination of the Actuator Power Consumption and System Energy Transfer. J Intell Mater Syst Struct 1994;5:12–20. https://doi.org/10.1177/1045389X9400500102.

[4] M. V. Gandhi, B. S. Thompson. Smart materials and structures 1992. https://doi.org/10.1002/adma.19930050427.

[5] Sha X, Zhu S. A Baseline-Free Electromechanical Impedance Resonance Method for Measuring the Modulus of Elasticity of Concrete Cubes Using Surface-Bonded PZT Patches. Struct Control Health Monit 2024;2024. https://doi.org/10.1155/2024/6153935.

[6] T. Jothi Saravanan , N. Gopalakrishnan, C. Bharathi Priya. Monitoring of early-age characteristics of concrete using EMI based embedded PZT transducers on varying plate thickness. International Conference on Advances in Construction Materials and Systems (ICACMS-2017) with 71st RILEM, Chennai, India: 2017.

[7] Jothi Saravanan T, Singh Chauhan S. Study on pre-damage diagnosis and analysis of adhesively bonded smart PZT sensors using EMI technique. Measurement (Lond) 2022;188. https://doi.org/10.1016/j.measurement.2021.110411.

[8] Bhalla S, Soh CK. Electromechanical Impedance Modeling for Adhesively Bonded Piezo-Transducers. J Intell Mater Syst Struct 2004;15:955–72. https://doi.org/10.1177/1045389X04046309.

[9] Tawie R, Lee HK. Monitoring the strength development in concrete by EMI sensing technique. Constr Build Mater 2010;24:1746–53. https://doi.org/10.1016/j.conbuildmat.2010.02.014.

[10] Shin SW, Oh TK. Application of electro-mechanical impedance sensing technique for online monitoring of strength development in concrete using smart PZT patches. Constr Build Mater 2009;23:1185–8. https://doi.org/10.1016/j.conbuildmat.2008.02.017.

[11] Lu X, Lim YY, Soh CK. Investigating the performance of "Smart Probe" based indirect EMI technique for strength development monitoring of cementitious materials – Modelling and parametric study. Constr Build Mater 2018;172:134–52. https://doi.org/10.1016/j.conbuildmat.2018.03.222.

[12] Shin SW, Qureshi AR, Lee J-Y, Yun CB. Piezoelectric sensor based nondestructive active monitoring of strength gain in concrete. Smart Mater Struct 2008;17:055002. https://doi.org/10.1088/0964-1726/17/5/055002.

[13] Jena T, Raj AK, Saravanan TJ, Bansal T. Deep learning neural networks for monitoring early-age concrete strength through a surface-bonded PZT sensor configuration. Measurement 2025;241:115698. https://doi.org/10.1016/j.measurement.2024.115698.

[14] Jothi Saravanan T, Balamonica K, Bharathi Priya C, Gopalakrishnan N, Murthy SGN. Piezoelectric EMI–Based Monitoring of Early Strength Gain in Concrete and Damage Detection in Structural Components. Journal of Infrastructure Systems 2017;23. https://doi.org/10.1061/(ASCE)IS.1943-555X.0000386.

[15] Bharathi Priya C, Jothi Saravanan T, Balamonica K, Gopalakrishnan N, Rao ARM. EMI based monitoring of early-age characteristics of concrete and comparison of serial/parallel multi-sensing technique. Constr Build Mater 2018;191:1268–84. https://doi.org/10.1016/j.conbuildmat.2018.10.079.

[16] Annamdas VGM, Rizzo P. Monitoring concrete by means of embedded sensors and electromechanical impedance technique. In: Tomizuka M, editor., 2010, p. 76471Z. https://doi.org/10.1117/12.847687.

[17] Yang Y, Divsholi BS, Soh CK. A Reusable PZT Transducer for Monitoring Initial Hydration and Structural Health of Concrete. Sensors 2010;10:5193–208. https://doi.org/10.3390/s100505193.

[18] T. T. Nguyen, J. T. Kim, Q. B. Ta, D. D. Ho, T. T. V. Phan, T. C. Huynh. Deep learning-based functional assessment of piezoelectric-based smart interface under various degradations. Smart Struct Syst 2021;28:69–87.

[19] Huynh T-C, Nguyen T-D, Ho D-D, Dang N-L, Kim J-T. Sensor Fault Diagnosis for Impedance Monitoring Using a Piezoelectric-Based Smart Interface Technique. Sensors 2020;20:510. https://doi.org/10.3390/s20020510.

[20] Bansal T, Azam A, Morwal T, Talakokula V, Jothi Saravanan T. Assessing cement paste strength evolution under curing: An experimental and numerical investigation through equivalent stiffness parameter identified by embedded piezo sensors. Measurement 2025;241:115713. https://doi.org/10.1016/j.measurement.2024.115713.

[21] Jena T, Saravanan TJ, Bansal T. Deep Learning-based data-driven technique for early-age concrete strength monitoring using the non-bonded piezoelectric sensor system. Measurement 2025;256:118346. https://doi.org/10.1016/j.measurement.2025.118346.

[22] Sun FP, Chaudhry ZA, Rogers CA, Majmundar M, Liang C. Automated real-time structure health monitoring via signature pattern recognition; In: Chopra I, editor., 1995, p. 236–47. https://doi.org/10.1117/12.208261.

[23] Park G, SH, FCR and IDJ. Overview of Piezoelectric Impedance-Based Health Monitoring and Path Forward. The Shock and Vibration Digest 2003;35:451–63.

[24] Bhalla S, Soh CK. High frequency piezoelectric signatures for diagnosis of seismic/blast induced structural damages. NDT & E International 2004;37:23–33. https://doi.org/10.1016/j.ndteint.2003.07.001.

[25] Bansal T, Talakokula V, Mathiyazhagan K. Equivalent structural parameters based non-destructive prediction of sustainable concrete strength using machine learning models via piezo sensor. Measurement 2022;187:110202. https://doi.org/10.1016/j.measurement.2021.110202.

[26] Soh CK, Bhalla S. Calibration of piezo-impedance transducers for strength prediction and damage assessment of concrete. Smart Mater Struct 2005;14:671–84. https://doi.org/10.1088/0964-1726/14/4/026.

[27] Talakokula V, Bhalla S, Gupta A. Monitoring early hydration of reinforced concrete structures using structural parameters identified by piezo sensors via electromechanical impedance technique. Mech Syst Signal Process 2018;99:129–41. https://doi.org/10.1016/j.ymssp.2017.05.042.

[28] Moharana S, Bhalla S. Development and evaluation of an external reusable piezo-based concrete hydration-monitoring sensor. J Intell Mater Syst Struct 2019;30:2770–88. https://doi.org/10.1177/1045389X19873414.

[29] Bansal T, Talakokula V. Deterioration of structural parameters due to corrosion in prestressed concrete identified by smart probe-based piezo sensor. Engineering Research Express 2021;3:015011. https://doi.org/10.1088/2631-8695/abded9.

[30] Bansal T, Talakokula V, Sathujoda P. Durability aspects of blended concrete systems subjected to combined mechanical and environmental loading using piezo sensor. Constr Build Mater 2022;348:128613. https://doi.org/10.1016/j.conbuildmat.2022.128613.

[31] Bansal T, Talakokula V. Study of Durability Aspects of Limestone Calcined Clay Cement Using Different Piezo Configurations. vol. 25. Springer. Singapore: 2020.

[32] E.L. Hixon. Mechanical Impedance. 3rd ed. NewYork: Mc Graw Hill Book; 1998.